How pure mode I can be obtained in bi-material bonded DCB joints: a longitudinal strain-based criterion

Wandong Wang[a,b,*], Romina Lopes Fernandes[a,b], Sofia Teixeira De Freitas[b], Dimitrios Zarouchas[b], Rinze Benedictus[b]

[a] *Co-first author: These authors contributed equally to this work*
[b] *Structural Integrity & Composites Group, Faculty of Aerospace Engineering, Delft University of Technology, P.O. Box 5058, 2600 GB Delft, The Netherlands*

Abstract

An essential question to predict the structural integrity of bi-material bonded joints is how to obtain their fracture properties under pure mode I. From open literature, it is found that the most commonly used design criterion to test mode I fracture is matching the flexural stiffnesses of the two adherents in a DCB coupon. However, the material asymmetry in such designed joints results in mode II fracture as well. In this paper, a new design criterion is proposed to obtain pure mode I fracture in adhesively bonded bi-material DCB joints by matching the longitudinal strain distributions of the two adherends at the bondline - longitudinal strain based criterion. A test program and Finite Element modelling have been carried out to verify the proposed design criterion using composite-metal bonded DCB joints. Both the experimental and numerical results show that pure mode I can be achieved in bi-material joints designed with the proposed criterion. $G_{\mathrm{II}}/G_{\mathrm{I}}$ ratio is reduced by a factor of 5 when using the proposed longitudinal strain based criterion in comparison with the flexural stiffness based criterion.

Keywords: bi-material DCB, Pure mode I fracture, fracture toughness, dissimilar adherends

1. Introduction

The use of fibre reinforced polymer composites has been steadily increasing in structural applications thanks to the many advantages they offer, such as high strength to weight ratio, tailorability, superior fatigue resistance, potential weight saving. Interests in joining composite materials to metals have also arisen in aeronautic, automotive and civil industries to take advantage of both advanced composites and traditional metals, resulting in bi-material composite-metal structures[1–4].

Adhesive bonding technique is the most suitable joining technique in terms of weight and performance to join composites to metals, and it has been widely applied in many industrial sectors [5, 6]. Compared to conventional mechanically fastened joining method, an identified advantage of using adhesive bonding for composite materials is eliminating fastener holes and fasteners, which provide the chance of weight saving and extended fatigue life [7, 8]. On the other hand, adhesive bonding requires an expensive autoclave curing process, proper surface preparation and can be sensitive to aggressive environment and high temperature.

The lack of knowledge and predictive methods about fracture and fatigue behaviour of adhesively bonded structures, compared to the well-established damage tolerance analysis for mechanically fastened structures, is one of the main reasons that limit the extensive application of adhesively bonded structures [9]. The interfacial fracture in adhesively bonded joints is commonly a combination of three fracture modes: opening mode I, in-plane share mode II and out-of-plane share mode III. In Fig. 1 the three fracture modes are

*Corresponding author. *Tel.:* +31 (0)15 278 9748;
E-mail address: w.wang-3@tudelft.nl, wwandong@gmail.com

schematically illustrated. In this research, the characterization of pure mode I of bi-material bonded joints will be addressed.

Currently, standard mode I fracture test methods are only available for joints with the same adherend material. The Double Cantilever Beam (DCB) fracture test is typically used to obtain mode I fracture toughness of bonded joints [10]. Experimental and numerical work has been carried out by many researchers for bonded joints with symmetric DCB (same material and same thickness) configuration [11–15].

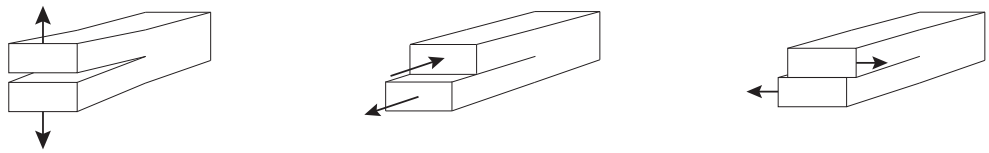

(a) mode I: opening. (b) mode II: in-plane shear. (c) mode III: out-of-plane shear.

Figure 1: The three fracture modes.

However, the fracture behaviour and correspondent critical fracture energy might be dependent on the materials of two adherends when performing fracture test of bi-material DCB joints. In this case, the standard DCB specimen has to be adapted. From open literature, it is found that, for bi-material DCB joints, the most commonly used design criterion is matching the flexural stiffnesses of the two adherends [1, 16–18]. Although the flexural deformation of two adherends is symmetric in the bi-material DCB specimen designed with this criterion, mode II fracture component has been found [1, 17]. Ouyang et al. [19] has reported that the shear stress in the adhesive interlayer between two dissimilar adherends has to be suppressed to obtain pure mode I, otherwise mode II would be present. Zambelis et al. [20] has verified the idea of Ouyang with numerical simulation. Therefore, a new design criterion to achieve pure mode I in a bonded bi-material joint is needed.

In this paper, a new design criterion is proposed to obtain pure mode I fracture in adhesively bonded bi-material DCB joints by matching the longitudinal strain distributions of the two adherends at the bondline - longitudinal strain based criterion. This criterion is validated with an experimental and numerical case study using adhesively bonded composite-to-metal DCB joint configuration.

2. Proposed approach

Consider cohesive failure in bonded bi-material DCB joints, the crack is embedded within the adhesive interlayer between two adherends. According to Williams [21], one of the three fracture modes illustrated in Fig. 1 can only arise when there is a mismatch in strains at the crack tip in the correspondent mode. In order to develop a method of achieving pure mode I in an adhesively bonded joint with the adhesive layer embracing a crack, it is crucial to examine the deformation of the cracked adhesive layer especially around the crack tip.

2.1. Analysis of the deformation of the cracked adhesive layer in a bi-material DCB specimen

In a DCB specimen, the loading applied to the adhesive layer is introduced by the deformation of the two adherends. In Fig. 2, a general DCB specimen with dissimilar adherends is schematically illustrated. The flexural longitudinal modulus and thickness of the upper and lower beams are denoted as E_1, h_1 and E_2 h_2, respectively. The two beams open up under a pair of opening loading P, however the two beams are not perfectly cantilevered at the crack tip [10]. A portion of adhesive is deformed in front of the crack tip. The deformation of the adhesive layer containing the crack is governed by the displacement of the lower surface of the upper beam and the displacement of the upper surface of the lower beam, as illustrated in the closeup crack picture shown in Fig. 2.

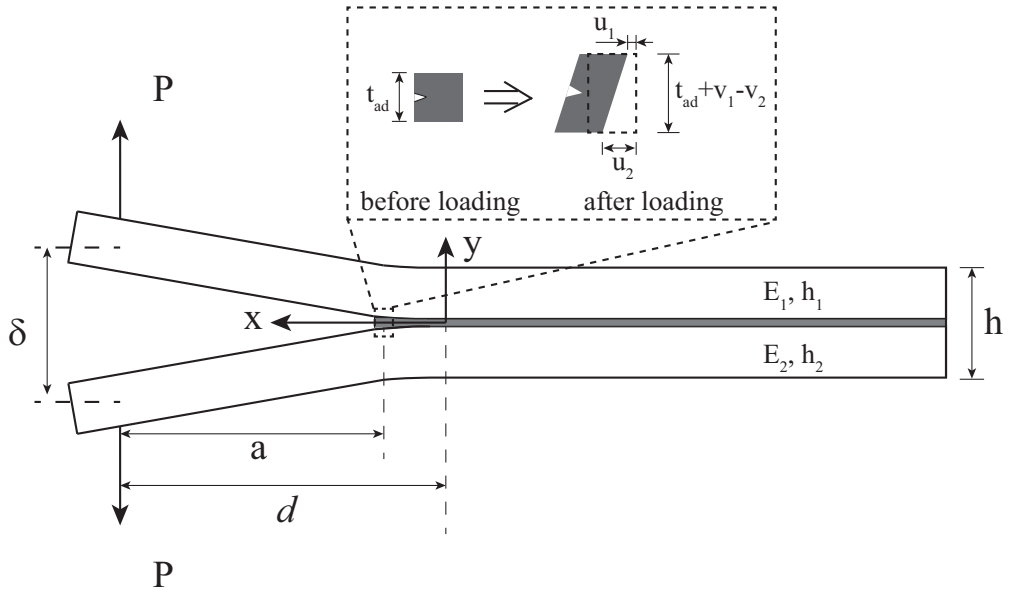

Figure 2: Deformation of the cracked adhesive in the DCB specimen.

It is therefore crucial to analyse the deformation of the two beams of the DCB joint to extract the displacements of the faying surfaces. In the proposed approach, it is assumed that linear elastic fracture mechanics is applicable. Therefore the classic beam theory is employed to derive the deformations of the two beams. The origin of the X-Y coordinates is set at the point where the two beams are built in, see Fig. 2. The exact location is unknown, since it is highly dependent on the mechanical properties of the adhesive system, but it is not required to explain the fracture modes in the adhesive layer.

The longitudinal displacement in x-direction and vertical displacement in y-direction of the lower surface of the upper beam developed from the simple beam theory are given by

$$u_1 = \frac{Ph_1}{2E_1I_1}(d-x)x \tag{1}$$

$$v_1 = \frac{P}{E_1I_1}(\frac{dx^2}{2} - \frac{x^3}{6}) \tag{2}$$

and similarly the corresponding displacements of the upper surface of the lower beam are expressed as

$$u_2 = \frac{Ph_2}{2E_2I_2}(d-x)x \tag{3}$$

$$v_2 = -\frac{P}{E_2I_2}(\frac{dx^2}{2} - \frac{x^3}{6}) \tag{4}$$

where P is the applied load, d is the distance between the load line and y-axis. I is the moment of inertia and is given by Eq. 5 for the beam with a rectangular cross section of width b and thickness h. The subscripts 1 and 2 refer to the upper and lower beams, respectively.

$$I = \frac{1}{12}bh^3 \tag{5}$$

With the small deformation assumption, the normal strain, ϵ_{yy}, and shear strain, γ_{xy}, of the adhesive layer can be derived respectively as following:

$$\epsilon_{yy} = \frac{v_1 - v_2}{t_{ad}} \tag{6}$$

$$\gamma_{xy} = \frac{u_1 - u_2}{t_{ad}} \tag{7}$$

where t_{ad} denotes the thickness of the adhesive layer.

Eq. 6 indicates that the adhesive layer containing a crack deforms in opening mode. While Eq. 7 shows that an in-plane-shear mode could occur. These strains are illustrated schematically in Fig. 2.

It is evident that the reaction forces from the adhesive on the beams are not considered in calculating the displacements of the faying surfaces. Consequently the above obtained strains are a first approximation of strains of the adhesive. Nevertheless, they provide the tendency of how the cracked adhesive layer could deform. The significance of accounting the reaction forces in the calculation is discussed in the next subsection.

2.2. Criterion to achieve pure mode I

Based on the analysis of the deformation of the cracked adhesive layer in a general bi-material DCB specimen, it has shown that the existence of shear deformation of the adhesive layer with a crack introduces in-plane-shear fracture mode, i.e. mode II. In order to obtain pure mode I in such a DCB specimen, the shear strain in the cracked adhesive should be eliminated, i.e. $\gamma_{xy} = 0$. The following equation can then be obtained based on Eq. 7:

$$u_1 = u_2 \tag{8}$$

The longitudinal strain distributions of the faying surfaces can be determined by the displacement distribution with Eq. 8. Eq. 8 can be rewritten in terms of strain, which is expressed as Eq. 10:

$$\epsilon = \frac{\partial u}{\partial x} \tag{9}$$

$$\epsilon_1 = \epsilon_2 \tag{10}$$

In order to eliminate the shearing mode in the DCB specimen, the longitudinal strain distributions at the two faying surfaces should be identical. If this criterion is fulfilled, only pure mode I fracture will develop in the adhesive with the crack. If this criterion is not satisfied, the mismatch of strains of the faying surfaces will lead to mode II fracture behaviour [21].

The DCB specimen with dissimilar adherends should be designed to meet this criterion under a pair of applied loads. Substituting Eq. 1, Eq. 3 and Eq. 5 into Eq. 8, one can obtain the following equation:

$$E_1 h_1^2 = E_2 h_2^2 \tag{11}$$

If a bi-material DCB specimen is designed according to Eq. 11, the faying surfaces of the two beams under a pair of applied load, as illustrated in Fig. 2, would have identical longitudinal displacements and strain distributions. There is no tendency of loading the adhesive layer in shear mode. The adhesive layer is expected to deform only in y-direction. Consequently, the reaction forces from the adhesive layer on the beams are in y-direction only.

Assuming that the reaction forces acting on the beam surfaces follow a similar distribution $f(x)$, as illustrated in Fig. 3, the moment distributions over the deformed adhesive layer region for the two beams can be given by:

$$-M_1 = M_2 = \int_0^x f(x) x dx \tag{12}$$

Under the reaction force distributions from the adhesive, the longitudinal displacements can be given by:

$$u_{r1} = \frac{h_1 x M_1}{2 E_1 I_1} = -\frac{6x \int_0^x f(x) x dx}{E_1 h_1^2 b} \tag{13}$$

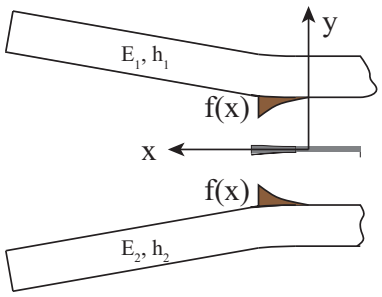

Figure 3: Illustration of the reaction force distributions from the adhesive layer on the beams of the DCB specimen.

$$u_{r2} = -\frac{h_2 x M_2}{2E_2 I_2} = -\frac{6x\int_0^x f(x)xdx}{E_2 h_2^2 b} \tag{14}$$

Giving the fact that Eq. 11 is valid, these two longitudinal displacements caused by the reaction forces are identical. Based on the analysis above, no shearing could be involved. It has been proven that pure mode I in the DCB specimen with two beams of different materials could be obtained when the design criterion of Eq. 11 is met.

The two beams of a DCB specimen with the matched strain distributions do not necessarily deform symmetrically under a pair of opening load. In order to have symmetric deformation of the DCB beams, the flexural or bending stiffness of the two beams should be equal, then $E_1 h_1^3 = E_2 h_2^3$ is satisfied. However, this configuration involves mode II fracture behaviour [1, 17].

If DCB specimens are made of the same material, pure mode I can be obtained if the thickness of the two beams is the same, because $E_1 h_1^2 = E_2 h_2^2$ and $E_1 h_1^3 = E_2 h_2^3$ are equally met. However for bi-material DCB specimens, these two criteria cannot be met simultaneously. In this case, the strain-based criteria is the one to be chosen if one aims for pure mode I.

2.3. Design of the composite adherend

In the preceding subsections, the effective flexural modulus of the adherend is used. For isotropic materials, such as metals, the flexural modulus is equal to the material's Young's modulus. However, for composite laminates this is not the case. In this paper, the flexural modulus of composite laminates is determined using the Classic Laminate Theory (CLT).

According to the CLT, an ABD-matrix can be developed for a composite laminate [22]. The ABD-matrix can be used to calculate the middle plane strains $[\varepsilon^0]$ and curvatures $[\bar{k}]$ as a result of applied line loads $[N]$ and moments $[M]$ as following:

$$\begin{bmatrix} \varepsilon^0 \\ \bar{k} \end{bmatrix} = \begin{bmatrix} A & B \\ B & D \end{bmatrix}^{-1} \begin{bmatrix} N \\ M \end{bmatrix} = \begin{bmatrix} A^* & B^* \\ C^* & D^* \end{bmatrix} \begin{bmatrix} N \\ M \end{bmatrix} \tag{15}$$

and the laminate strains throughout thickness can be calculated as

$$\begin{bmatrix} \varepsilon_x \\ \varepsilon_z \\ \gamma_{xz} \end{bmatrix} = \begin{bmatrix} \varepsilon_x^0 \\ \varepsilon_z^0 \\ \gamma_{xz}^0 \end{bmatrix} + y \begin{bmatrix} \bar{k}_x \\ \bar{k}_z \\ \bar{k}_{xz} \end{bmatrix} \tag{16}$$

where y is in the direction of thickness with its origin at the middle plane and x and z are longitudinal and transverse axes, respectively. In this paper, the strains at the faying surface of the composite adherend need to be determined. For this, $y = h/2$ should be substituted into Eq. 16 to obtain the corresponding strains.

Based on Eq. 15, the relation between the longitudinal curvature $\bar{k}_x$ and moment M_x is

$$\bar{k}_x = D_{11}^* M_x \tag{17}$$

where D^*_{11} is the element at the first row and first column of $[D]^*$. Therefore, the longitudinal flexural stiffness E^f_x can be derived:

$$E^f_x = \frac{12M_x}{\bar{k}_x h^3} = \frac{12}{h^3 D^*_{11}} \tag{18}$$

The longitudinal flexural stiffness E^f_x is only valid for symmetric laminates. Analogous to the calculation of the longitudinal strain throughout thickness for isotropic metals, the longtitudinal strain of symmetric composite laminate can then be easily determined by

$$\epsilon_x = \frac{M_x y}{E^f_x I} \tag{19}$$

Based on Eq. 18, the proposed criterion expressed as Eq. 11 can be used to obtain the desirable layup of the composite adherend.

For an asymmetric composite laminate, the longitudinal strain cannot be calculated directly using Eq. 19. This is attributed to the fact that $[\varepsilon^0] \neq [0]$. In this case, Eq. 16 has to be used to obtain the longitudinal strain of an asymmetric laminate, such that the longitudinal strain at the faying surface is equal to the strain at the faying surface of the opposite adherend.

3. Case study

A test program was carried out in order to validate the proposed approach of achieving pure mode I in DCB specimens made of dissimilar materials. The DCB specimens were made out of Steel strips bonded to Glass Fibre Reinforced Polymer (GFRP) laminates. Two DCB configurations were manufactured: one batch following the Strain based design criterion $E_1 h_1^2 = E_2 h_2^2$ and one batch following the Curvature based criterion $E_1 h_1^3 = E_2 h_2^3$. Both specimens configurations were tested and numerically modelled.

Furthermore, symmetric Steel-Steel DCB specimens were manufactured in order to have a reference test. The fracture surfaces of the bi-material specimens were analysed and compared with the reference case.

3.1. Materials and specimens

Fig. 4 shows the DCB test specimen hybrid geometry which is characterised by adherends height h_{Steel} and $h_{\text{Composite}}$, adherends length L and width B, and an initial crack length a_0.

DCB specimens were manufactured by bonding Steel S690 and GFRP laminates using the structural epoxy adhesive Araldite 2015 (Huntsman®). The GFRP laminates were manufactured with quadraxial E-glass fabric, which consists of a stacking of four unidirectional (UD) layers of E-glass lamina with the orientations $-45°/90°/+45°/0°$, as shown in Fig. 5. The fabric nominal thickness is 0.9 mm. The laminates were manufactured by vacuum infusing the fabric stacking sequence with a rubber modified epoxy based vinyl ester resin. The laminates were cured for 24h at room temperature and post-cured for 12h at 60°C in an oven. The mechanical properties of UD-0° E-glass lamina, Steel and the epoxy adhesive are summarized in Table 1.

As aforementioned, two DCB configurations were manufactured: one following the Strain based design criterion and another following the Curvature based design criterion. In order to provide a better comparison of the results of the two configurations, the steel adherend was kept the same for all tested configuration and the GFRP adherend was designed to meet the individual design criterion by changing the stacking sequence of the GFRP laminates.

Table 2 shows the lay-up and thicknesses of the two configurations. The steel thickness of 3 mm was selected to avoid yielding during quasi-static fracture testing (this was numerically verified). For this given thickness of steel, the lay-up of the GFRP corresponding to each criterion is given in Table 2 column number 2. Unfortunately, neither criteria can be perfectly satisfied due to the fixed stacking sequence and thickness of the quadraxial E-glass fabric and available steel plate thicknesses. The final laminate thickness after curing is listed in Table 2 column number 3 (the final thickness is smaller than the nominal one due to the manufacturing process constraints). Finally, the theoretical thickness of the steel adherend which matches

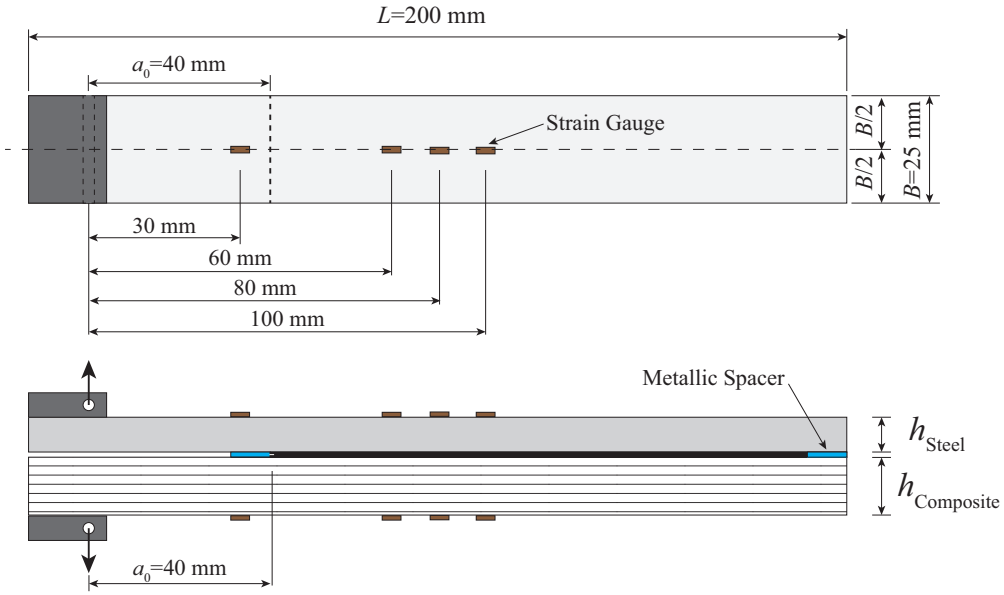

Figure 4: Steel-Composite Double Cantilever Beam (DCB) test specimen.

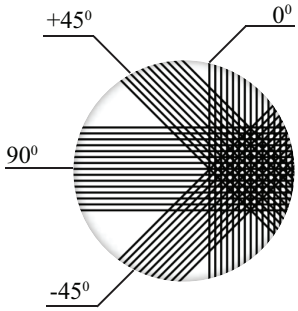

Figure 5: Quadraxial E-glass fabric representation: stacking of four UD layers E-glass lamina $-45°/90°/+45°/0°$.

Table 1: Material mechanical properties.

Material	E_1 (MPa)	E_2 (MPa)	G_{12} (MPa)	υ_{12}
UD-0° E-glass lamina	38070	11160	3951	0.28
Steel S690	210000		-	0.3
Epoxy adhesive [23]	2000		-	0.33

Axis 1: longitudinal/fibres direction; Axis 2: tranverse direction

perfectly to the real laminate configuration and the corresponding criterion is also provided in Table 2 (theoretical thickness).

Prior to bonding, the surfaces of steel and GFRP adherends were pretreated. All the bonded steel surfaces were sandblasted using aluminium oxide. Before and after sandblasting, the steel surfaces were cleaned with

Table 2: GFRP laminates: lay-up stacking for each design criterion (the lay-up is defined from the bottom to the top of the laminate).

Criterion	Lay-up	$h_{\text{Composite}}$ [mm]	h_{Steel} [mm] (theoretical thickness)	E_x^f [MPa]
Strain based	$[0^\circ\ +45^\circ\ 90^\circ\ -45^\circ]_5/[+45^\circ\ 90^\circ\ -45^\circ\ 0^\circ]_5$	8.60	3.00 (2.72)	21014
Curvature based	$[0^\circ\ +45^\circ\ 90^\circ\ -45^\circ]_4/[+45^\circ\ 90^\circ\ -45^\circ\ 0^\circ]_3$	6.06	3.00 (2.84)	21609

*Final thickness of the laminates after curing cycle

a clean cloth soaked with acetone. As a final step prior to bonding, the steel surfaces were cleaned by immersion for 10 min in an alkaline-cleaner and coated with a silane γ-glycidoxypropyltrimethoxysilane (γ-GPS) solution. A potassium hydroxide solution stirred at 300 rpm and heated to 60°C was used for the alkaline cleaning. The silane solution was prepared according to [24] and it is described hereafter. Firstly, the γ-GPS was hydrolysed in a Distilled Water (DIW)-Methanol mixture. The volume ratios of γ-GPS/DIW/Methanol were 10/80/10, respectively. The pH was set to a value of about 5 to 5.5 by adding acetic acid to maintain the solution stability. The solution was magnetically stirred for 48h at 300 rpm at room temperature. γ-GPS coatings were fabricated by immersing the steel adherends into the prepared silane solution for 20 seconds. Cure in an oven for 1h at 150°C took place afterwards. All the bonded GFRP laminates surfaces were manually sanded with grid240 sandpaper. During this process, care was taken to not affect the laminates' fibres. Before and after the sanding, the GFRP surfaces were cleaned with a clean cloth soaked with isopropanol.

A manual applicator gun with a static-mixing nozzle was used to mix and apply the two component epoxy paste adhesive Araldite® 2015. A certain quantity of adhesive was initially discarded to ensure a correct mixture of both components and to remove any bubbles which may have accumulated in the nozzle. The adhesive layer thickness was controlled by metallic spacers of 0.4 mm as shown in Fig. 4. The spacers were made out of 2 metallic stripes and a sharp razor blade, bonded by a fast curing glue. The razor blade was placed in between the metallic stripes (i.e., positioned at the mid thickness of the adhesive layer). A starter pre-crack was created in all specimens by the razor blade. All specimens, 5 DCB specimens per configuration, were cured in an oven for 1 hour at 80°C in accordance with the manufacturer's specifications. Weights were used to compress the specimens to guarantee a constant adhesive thickness of 0.4 mm. After curing, the adhesive thickness was measured according to ASTM standard [10] by measuring the total thickness of the specimens and substracting the adherends thicknesses.

Strains gauges were used in order to measure the longitudinal strains at the free surfaces of the specimens. A total of eight strain gauges were glued on each specimen (four on the steel adherend (type: KFG-5-120-C1-23), and the another four on the GFRP adherend (type: KFG-5-120-C1-11)). They were placed in specific locations as showed in Fig. 4.

A thin layer of white paint was applied to the side of the specimens in order to enhance visibility of the crack. Vertical lines every 1 mm were marked on the side in order to provide a length scale for the crack length measurements.

Symmetric Steel-Steel DCB specimens were also manufactured in order to obtain the fracture morphology of the adhesive under pure mode I loading. The bonding process described previously was followed.

3.2. Test set-up

Mechanical tests on DCB specimens were conducted based on ASTM standard test method D5528-13 [10]. The quasi-static tests were performed on a 20 kN (load-cell precision of 0.5%) Zwick tensile test machine under displacement control, with a fixed displacement rate of 1 mm/min (the displacement was measured by the testing machine itself and by two extensometers placed closer to the grips). The crack length was measured by means of a camera placed at the side of the specimen. Pictures were taken every second.

The crack length was defined as the distance between the load line and the crack tip, where the load line is assumed to be coincident with the centreline of the pins of the grips. The displacement used in

all calculations is the grip-to-grip displacement measured by the extensometers. It is assumed that any displacement occurring in the loading blocks is negligible compared to the deformation of the arms of the specimens.

Fig. 6 shows an overview of the experimental test set-up and a close-up view of the specimen under loading. It is possible to observe the extensometers, the loading blocks and the crack length at that moment of the test.

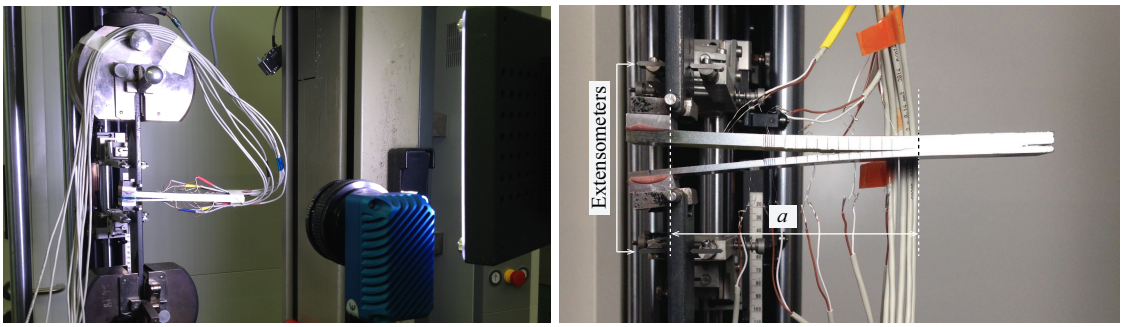

(a) Overview. (b) Close-up view of the experiment.

Figure 6: Test set-up.

4. Finite Element Modeling (FEM)

3D models were built in Abaqus® to model the fracture behaviour of the DCB tested joints. The Virtual Crack Closure Technique (VCCT) was used for calculation of the fracture parameters at the crack tip. The concept behind VCCT is based on the following - see Fig. 7: the strain energy released when the crack grows by the length of one element (Δa) is assumed to be equal to the energy required to close the crack by the same length. This energy is found by considering the work done by the forces at the crack tip node (node i, F_i) when displaced over a distance equal to the displacement of the nodes directly behind the crack tip (nodes j and k, U_j and U_k)[25, 26].

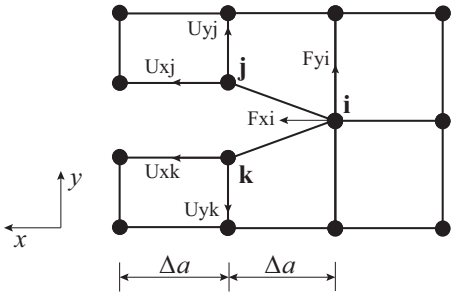

Figure 7: Nodes at the crack tip for VCCT in 2D FEM [26].

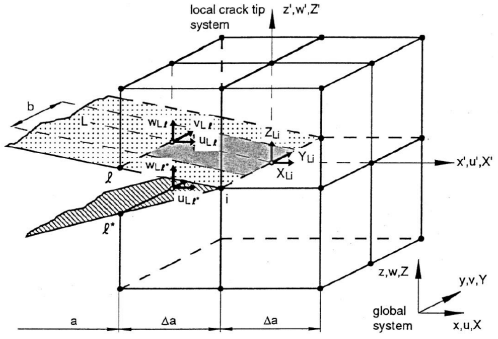

Figure 8: VCCT for 8-noded solid elements (lower surface forces are not represented for visual clarity) [27].

For a model with 8-noded 3D solid elements as shown in Fig. 8, the fracture components G_{I}, G_{II} and

G_{III} are calculated as,

$$G_{\mathrm{I}} = \frac{1}{2\Delta a.b}[Z_{Li}(w_{Ll} - w_{Ll^*})] \tag{20}$$

$$G_{\mathrm{II}} = \frac{1}{2\Delta a.b}[X_{Li}(u_{Ll} - u_{Ll^*})] \tag{21}$$

$$G_{\mathrm{III}} = \frac{1}{2\Delta a.b}[Y_{Li}(v_{Ll} - v_{Ll^*})] \tag{22}$$

where X_{Li}, Y_{Li} and Z_{Li} are the nodal forces at the node Li at the crack tip, and u_{Ll}, v_{Ll}, w_{Ll},u^*_{Ll}, v^*_{Ll}, w^*_{Ll} are the displacements of the top face and lower face adjacent nodes Ll and Ll^*, respectively. Δa is the increment of the crack which is equal to the element size at the crack tip and b is the width of the elements [26–28].

VCCT is implemented as a crack propagation tool in ABAQUS® which means that propagation only occurs when a certain criterion, e.g. Benzeggagh-Kenane law, exceeds a certain value, e.g. 1.0. In this study the FE model is used to obtain the fracture energy profiles at the crack tip line. Fracture energies values are given along the width of the specimen at the crack tip location for the three modes: mode I, II and III. The crack propagation prediction is not part of this study, since the aim is to evaluate the crack loading mode and not predict the damage progression. Hence, very high values were entered for the critical fracture components. This assured that the crack growth criterion would not reach the value of 1.0. A similar approach was used by Zarouchas and Alderliesten [29] where VCCT was employed to study how the size and the position of a defect alters the mode-mix ratio when an adhesively bonded stiffened panel is subjected to compression loading.

Fig. 9(a) shows a representation of the boundary conditions applied in the model. In order to simulate the real constraints during a DCB test, the following boundary conditions and loading were applied: the right end of the upper edge of the bottom adherend was constrained from all displacements. Rotations were not constrained. A load was applied on the right end of the upper edge of the top adherend, equal to the load taken from the experimental tests at specific crack length points ($Load_{\mathrm{i}} = f(a_{\mathrm{i}})$).

The specimens were modelled using 8 node linear brick elements (C3D8). In a 3D model, the Abaqus® integrated VCCT capability is only compatible with linear elements. The adhesive layer thickness was not explicitly modelled due to its negligible contribution to the overall specimen's stiffness in comparison with the adherends. All materials were modelled as linear elastic, using the materials properties given in Table 1.

The number of elements in thickness direction of the GFRP adherends was defined by one element per Quadraxial fabric. Taking into account each lay-up of the GFRP laminates, the following was defined: 10 elements for the Strain based approach, and 7 elements for the Curvature based approach. For the steel adherends, 8 elements were used in thickness direction for both criteria. The element size in width and length directions was set to $0.001B$ (B is the specimen width). A mesh convergence study was performed to guarantee mesh in-dependency of the numerical results. A 3D mesh overview is shown in Fig. 9(b).

5. Results and discussion

5.1. Experimental results and FEM validation

Fig. 10 shows the load-displacement curves of the Curvature based and Strain based criteria obtained during experiments. The linear part of these curves is compared with the linear elastic stiffness obtained from the numerical models. The FE model followed a similar stiffness as in the experiments.

There is an acceptable scatter in the experimental load-displacement curves for both configurations. One can also see that the maximum load of the Strain based specimens is higher than that of the Curvature based specimens. This difference was expected since the flexural stiffness of the composite adherend in the Strain based criterion is higher than that in the Curvature based criterion.

In order to further validate the FE model, the longitudinal strain values recorded by the strain gauges during experiments were compared to the correspondent numerical values obtained from the models. The

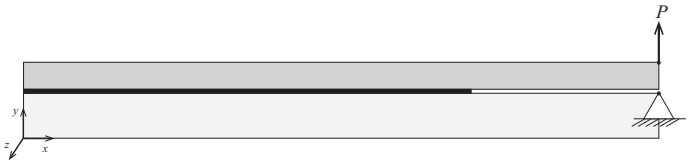

(a) Schematic representation of the boundary conditions. Note: The adhesive layer thickness is presented just for illustration purposes.

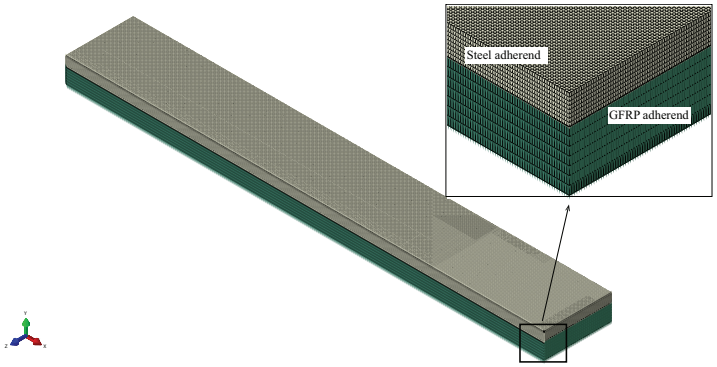

(b) Typical mesh of the numerical model, including a zoom of the specimen thickness.

Figure 9: DCB finite element model: boundary conditions and mesh overview.

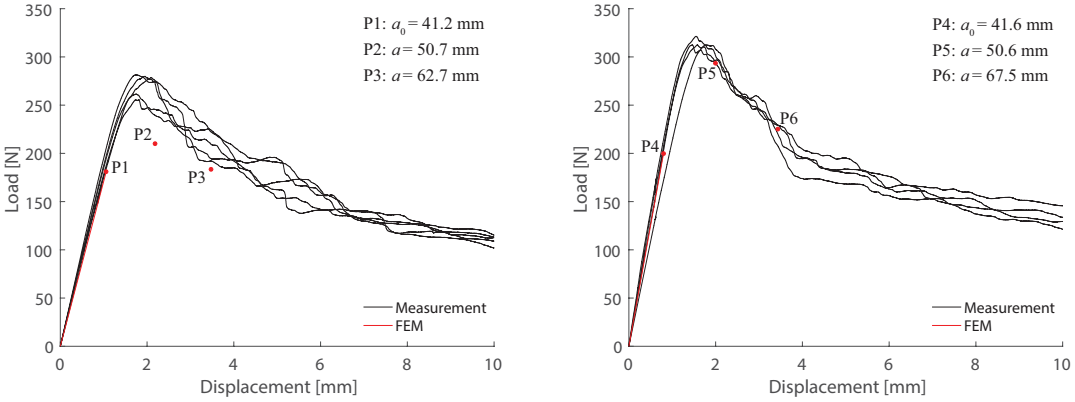

(a) Curvature based configuration

(b) Strain based configuration

Figure 10: FEM validation by using the initial linear part of the Load-displacement experimental curves for both configurations.

results are presented in Figs. 11 and 12 for Curvature and Strain based specimens, respectively. Three loading cases and correspondent crack lengths were considered for each criterion. These are represented in Fig. 10 by the points $P_{\text{i=1-6}}$. The x-position is defined from the load application point, as shown in the insert of Fig. 11(a). It can be observed that there is a good matching between the numerical and experimental longitudinal strain results.

Looking into more detail to the results presented in Figs. 11 and 12, one can observe two special features. Firstly, the longitudinal strains of both adherends did not become zero right in front of the crack tip. This shows that the two adherends were not perfectly cantilevered at the crack tip. The strains become zero about 10 mm ahead of the crack tip. Most likely the adhesive has deformed in this region. The second

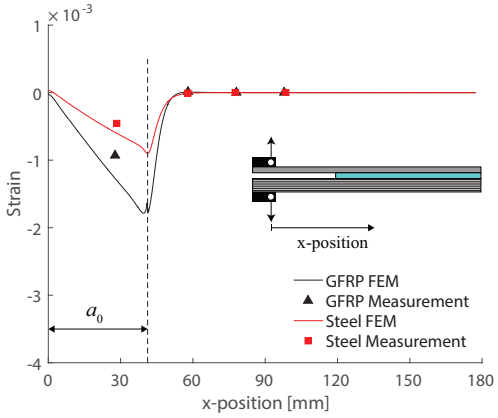

(a) **Point1**: P=181.09N $a_0 = 41.2mm$

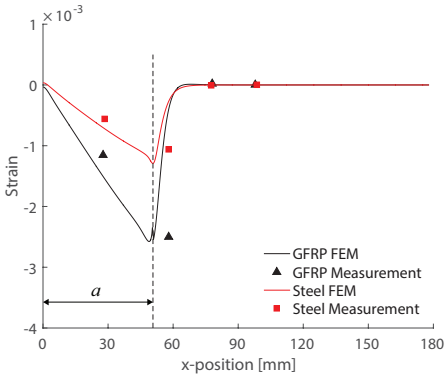

(b) **Point2**: P=210.32N $a = 50.7mm$

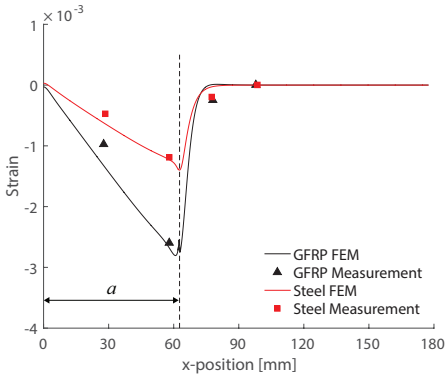

(c) **Point3**: P=183.59N $a = 62.7mm$

Figure 11: Curvature based criterion - Longitudinal strains as a function of the x-position for 3 different loading cases: numerical vs. experimental results.

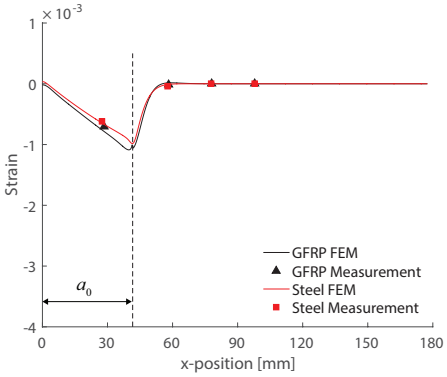

(a) **Point4**: P=200N $a = 41.6mm$

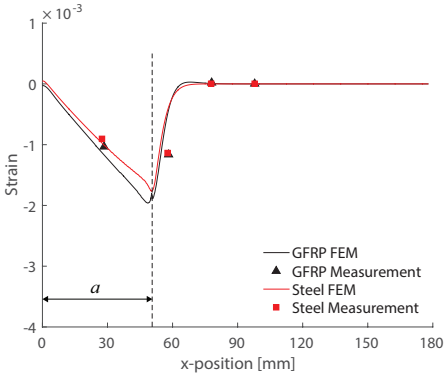

(b) **Point5**: P=293.48N $a = 50.6mm$

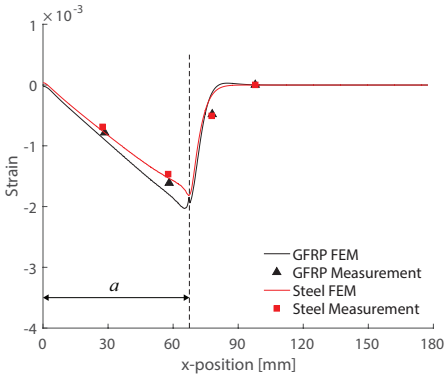

(c) **Point6**: P=225.26N $a = 67.5mm$

Figure 12: Strain based criterion - Longitudinal strains as a function of the x-position for 3 different loading cases: numerical vs. experimental results.

feature is related with the differences in the strain distributions of the two criteria. For the Curvature based specimens (Fig. 11), a great discrepancy in the strain distributions between the two adherends can be observed. Moreover, it is also shown that there was still some discrepancy in front of the crack tip, giving the indication that the adhesive in that region was loaded under shear mode. As expected, the strain

distributions were quite similar on both adherends for the proposed criterion (of matching the longitudinal strains at the bonded surfaces) - see Fig. 12. The slight difference still observed is attributed to the thickness manufacturing constraints inherent to both adherends.

This discussion is further supported with the fractography results of the tested two configurations, which is described in the next subsection.

5.2. Analysis of the fracture surfaces

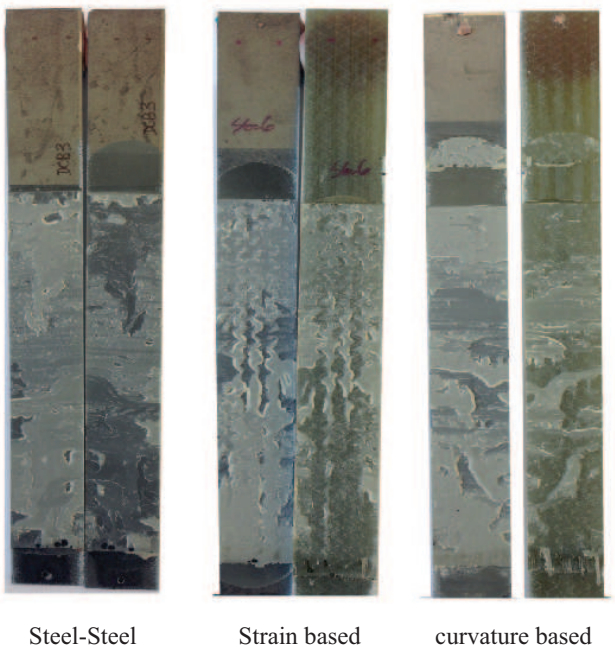

Figure 13: Representative macroscopic view of the fracture surfaces.

After testing, no delamination has been observed in the composite laminate. The fracture surfaces of all three tested configurations were analysed. A macroscopic view of the representative fracture surfaces is provided in Fig. 13. As can be seen, adhesive residues are clearly present on the pairs of adherends of all tested configurations, proving that all the specimens experienced cohesive failure during testing.

The fracture surfaces were also characterized at a microscopic level using JEOL JSM-7500F Field emission Scanning Electron Microscope (JEOL, Tokyo, Japan). This fractographic analysis was conducted to determine the failure modes in the tested DCB specimens. Prior to the SEM characterization, the fracture surface was visually observed and areas of interest were selected using optical microscopy. Interested areas were dissect from the adherends and inspected with SEM. Fig. 14 shows typical SEM microscopic fracture surfaces of all three tested configurations (5.0 kV acceleration voltage, Low angle secondary electron detector LEI): steel-steel, steel-composite strain based and steel-composite curvature based.

The failure took place in the bulky adhesive layer containing toughening particles, making interpretation of the fracture morphology more challenging [30]. The fracture morphology of such an adhesive system under pure mode I loading is extracted from the Steel-Steel DCB specimen, as shown in Fig. 14(a). This fracture surface is provided as a reference for pure mode I morphology features. The toughening particles were pulled apart directly from the resin without smearing it. Clear impressions of the toughening particles can be observed at the fracture surface shown in Fig. 14(a). These observations are clear evidences of the occurrence of pure mode I fracture [30].

Fig. 14(b) shows the typical fracture morphology of the strain based specimens and Fig. 14(c) shows the typical fracture morphology of the curvature based specimens. As can be seen, the fracture surface of the

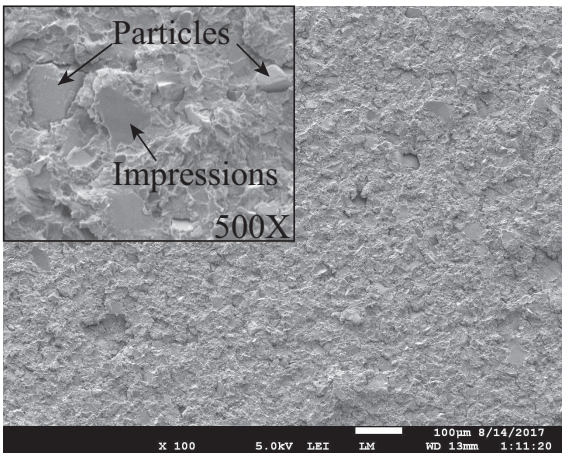

(a) Fracture surface of Steel-Steel specimen.

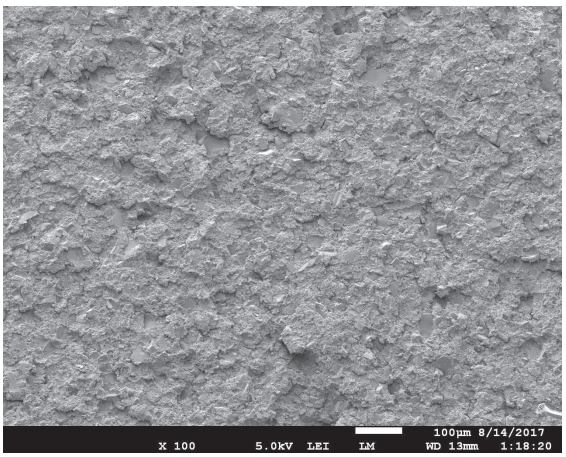

(b) Fracture surface of Strain based specimen.

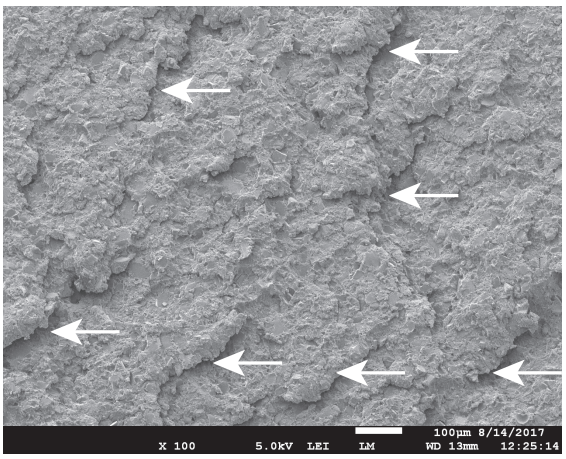

(c) Fracture surface of Curvature based specimen.

Figure 14: Fractography analysis. All pictures are taken at the magnification of 100X.

strain based specimen, shown in Fig. 14(b), is quite similar to that of the Steel-Steel specimen, whereas the fracture morphology of the curvature based specimen exhibits distinctly different features. Tilted cracks into the fracture surface indicated with white arrows in Fig. 14(c) can be observed. The occurrence of such tilted cracks indicates that mixed-mode failure took place in the curvature based specimens. The peeling stress and shear stress result in a principle tensile stress inclined at a certain angle to the global fracture surface, leading to tilted crack growth into the adhesive. The occurrence of shear stress can be explained with the difference in the strain distributions of the two adherends of curvature based specimens. Such features are hardly observed in Fig. 14(b), demonstrating the absence of mode II fracture in the strain based specimen.

The fractographic analysis shows that the failure modes in the strain based specimen comprise mode I while in the curvature based specimen comprise mode I and mode II. This analysis of the failure modes in the two configurations reaches the same conclusion discussed in subsection 5.1.

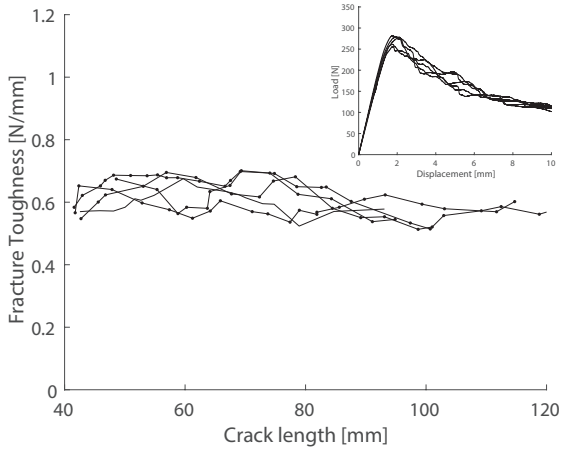

Figure 15: Fracture toughness of the Curvature based specimens.

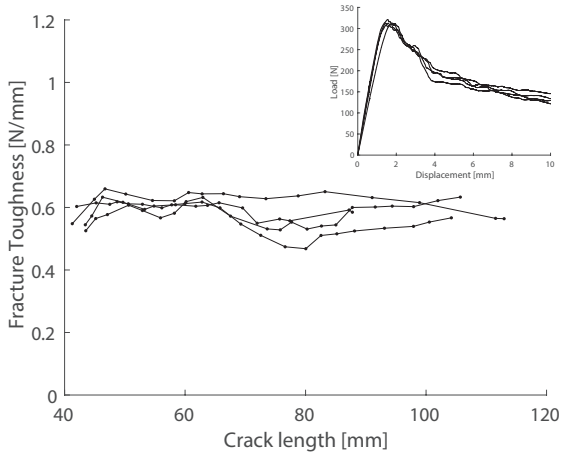

Figure 16: Fracture toughness of the Strain based specimens.

5.3. Critical fracture toughness results

The mode I fracture toughness of each tested DCB configuration was determined with the Modified Beam Theory (MBT) according to ASTM D5528-13 [10]. The fracture toughness is given by:

$$G_I = \frac{3P\delta}{2b(a + |\Delta|)} \tag{23}$$

where $|\Delta|$ is an experimentally determined crack length. According to the MBT, $|\Delta|$ denotes a portion of crack length which should be included into the actual crack length a when performing the calculation of G_{I} [10]. Experimentally determined, $|\Delta|$ is around 10 mm (at least 15 points were used to calculate $|\Delta|$ with an average R^2 of 0.9985 ± 0.0007).

For all the specimens, a *Resistance*-curve, also called R-curve, was obtained. This curve presents the fracture toughness as a function of the crack length. The experimental R-curves are presented in Figs. 15 and 16 for the Curvature based criterion and for the Strain based criterion, respectively. The critical fracture toughness was taken from the plateau on the R-curve. This plateau correspond to a stable crack propagation. As can be seen from Figs. 15 and 16, the fracture toughness for each configuration is around $0.6N/mm$. Due to the experimental scatter, it is hard to conclude that there is a well-marked difference in the values of

fracture toughness between the two configurations. However, it is understood so far that the curvature based specimens experienced mixed-mode fracture, and hence its fracture toughness parameters should not be carelessly calculated using Eq. 23.

Fig. 17 and 18 present the numerically calculated fracture toughness components for both criteria, Curvature based and Strain based respectively. For both configurations, mode I is dominant. On the other hand, mode II component is less pronounced and closer to 0 in the Strain based specimens when compared to the Curvature based specimens. The numerical results show that the Strain based criterion can provide better pure mode I in bi-material DCB specimens.

Due to the material limitation, it was unachievable to satisfy either criterion using the tested GFRP lay-up and steel. However, each criterion can be exactly met with the theoretical thickness of steel adherend provided in Table. 2. A numerical analysis was performed in order to examine the discrepancy in the $G_{\mathrm{II}}/G_{\mathrm{I}}$ ratios for both criteria when considering the experimental adherends' thicknesses (i.e. $h_{\mathrm{Composite}}$ and h_{Steel}) and the theoretical ones (i.e. $h_{\mathrm{Composite}}$ and Theoretical h_{Steel}). A load of 200N was applied and a crack of 41.6 mm was considered in both criteria. The results are presented in Fig. 19. One could see that by using the theoretical thicknesses, there is a reduction of mode II component. The $G_{\mathrm{II}}/G_{\mathrm{I}}$ ratio decreased from 6.1% to 3.5% for the Strain based criterion when considering the real and theoretical thicknesses, respectively. For the Curvature based case, these ratios are, as expected, higher ($G_{\mathrm{II}}/G_{\mathrm{I}}$ of 22.3% for the real thicknesses and $G_{\mathrm{II}}/G_{\mathrm{I}}$ of 18.6% for the theoretical ones). It is evident that the $G_{\mathrm{II}}/G_{\mathrm{I}}$ ratio is dramatically reduced, by a rough factor of 5, when the strain based criterion is followed to design the GFRP-Steel joint.

6. Applications and Limitations of the Strain based criterion

From the experimental and numerical results, one could see that, for the bi-material bonded joint studied, the mode II component is significantly suppressed by applying the Strain based criterion. In order to further investigate the applicability of this criterion to other bi-material joints, the authors have performed a numerical study to verify the influence of the adherend material on the $G_{\mathrm{II}}/G_{\mathrm{I}}$ ratio.

Table 3: Applicability of the Strain based criterion: joint types, materials, thicknesses and properties considered in the numerical models.

		Adherend 1		Adherend 2	
Joint Type	Materials	Thickness (mm)	Properties	Thickness (mm)	Properties
Benchmark	Steel-Steel	2.72046	$E = 210$ GPa $\upsilon = 0.3$	2.72046	$E = 210$ GPa $\upsilon = 0.3$
Asymmetric Isotropic-Isotropic	Steel-Aluminum	2.72046	$E = 210$ GPa $\upsilon = 0.3$	4.63323	$E = 74.2$ GPa $\upsilon = 0.33$
Asymmetric Isotropic-Symmetric Composite	Steel-Uni 0° GFRP	2.72046	$E = 210$ GPa $\upsilon = 0.3$	6.38942	$E_x^f = 38.07$ GPa $\upsilon_{12} = 0.28$
Asymmetric Isotropic-Asymmetric Composite	Steel-QE GFRP	2.72046	$E = 210$ GPa $\upsilon = 0.3$	8.6	$E_x^f = 21.014$ GPa $\upsilon_{12} = 0.28$

The studied cases are summarized in Table 3. All the cases have the same steel adherend (Adherend 1). The other adherend (Adherend 2) varies from isotropic metal to anisotropic composite materials. All the joints are designed following the Strain based criterion. The primary mechanical parameters are summarized in Table 3.

The $G_{\mathrm{II}}/G_{\mathrm{I}}$ ratios of the studied cases are presented in Fig. 20. It is noted that the $G_{\mathrm{II}}/G_{\mathrm{I}}$ ratio is dependent on the material of the Adherend 2. Compared to the asymmetric composite adherend, the symmetric unidirectional composite adherend provides lower $G_{\mathrm{II}}/G_{\mathrm{I}}$ ratio in the bi-material joint. This might be attributed to the elimination of the in-plane shear deformation. It is also observed that the $G_{\mathrm{II}}/G_{\mathrm{I}}$ ratio is lower for joints where the difference in the flexural stiffnesses of the two adherends is smaller, as for example for the Steel-Aluminium in comparison with Steel-Uni 0° GFRP. For the Steel-Aluminium joint,

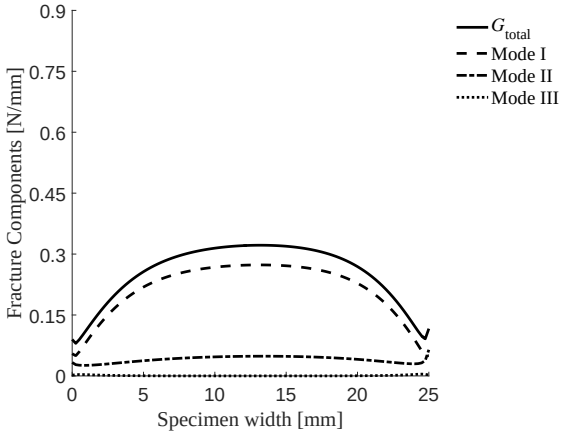

(a) **Point1**: P=181.09N $a_0 = 41.2mm$

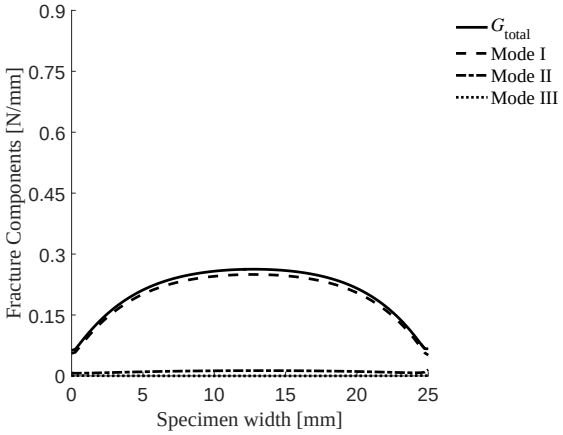

(a) **Point4**: P=200N $a = 41.6mm$

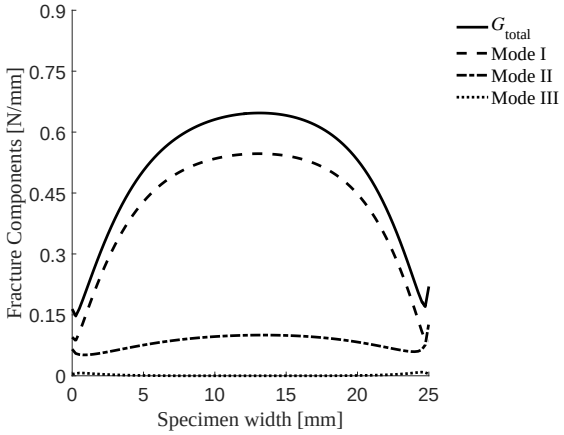

(b) **Point2**: P=210.32N $a = 50.7mm$

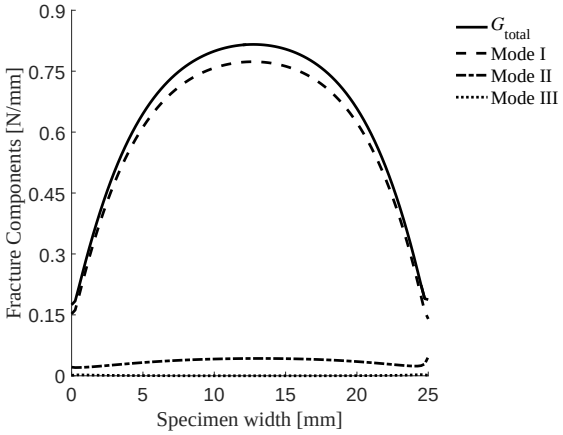

(b) **Point5**: P=293.48N $a = 50.6mm$

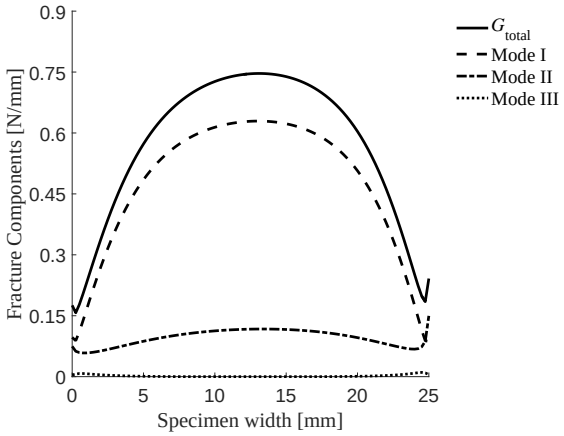

(c) **Point3**: P=183.59N $a = 62.7mm$

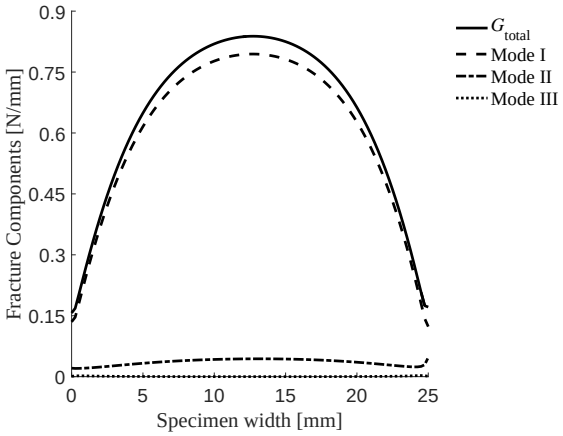

(c) **Point6**: P=225.26N $a = 67.5mm$

Figure 17: Curvature based criterion - Mode fracture components as a function of the specimen width for 3 different loading cases.

Figure 18: Strain based criterion - Mode fracture components as a function of the specimen width for 3 different loading cases.

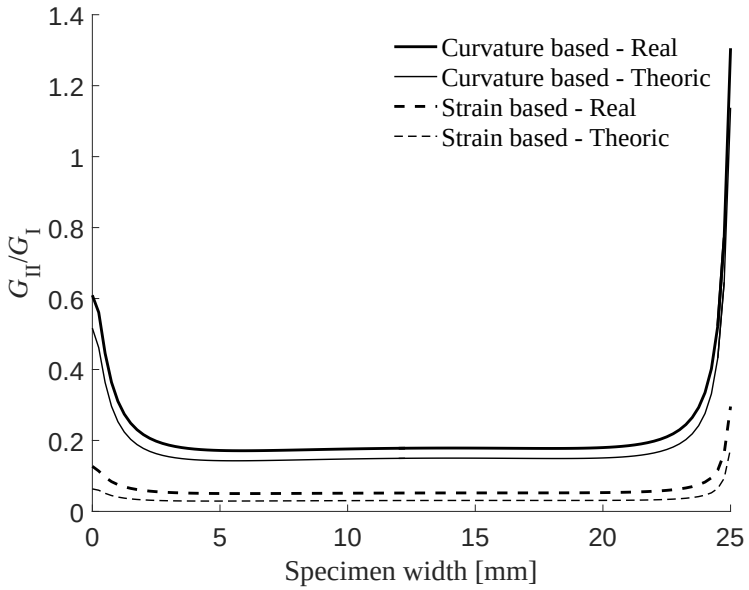

Figure 19: Comparison of the $G_{\mathrm{II}}/G_{\mathrm{I}}$ ratio for both criteria considering the real and theoretic thicknesses of the adherends.

the $G_{\mathrm{II}}/G_{\mathrm{I}}$ ratio is almost zero. This also shows that the criterion is not only for composite-metal but also metal-metal bi-material bonded joints.

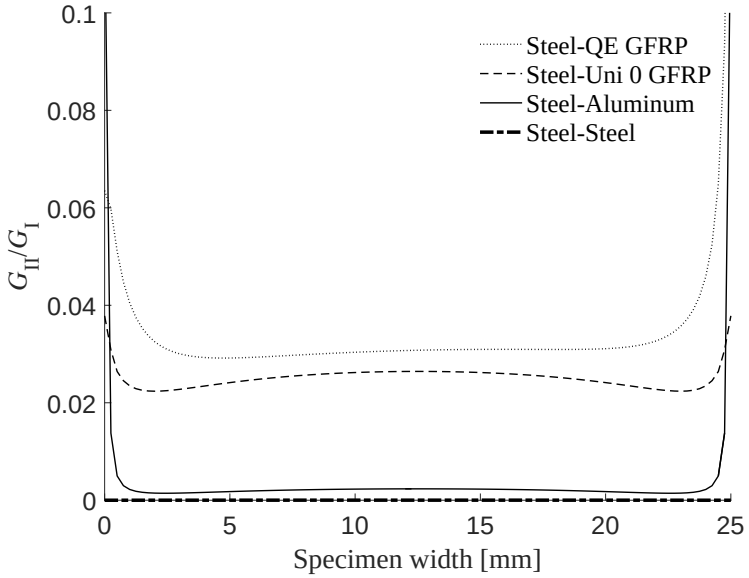

Figure 20: $G_{\mathrm{II}}/G_{\mathrm{I}}$ ratio of different bi-material bonded joints.

The authors are aware of certain limitations of the proposed strain based design criterion. First of all, the criterion does not account for the residual stresses in the adhesive interlayer due to the thermal coefficients mismatch of bonded bi-material adherends where the adhesive needs to be cured at higher temperature. The residual stresses may introduce certain mode-mixity. Another limitation is with regards to the in-plane shear deformation induced by the asymmetric lay-up of a composite adherend. It is suggested to use symmetric composite lay-up for testing bi-material joints. One more limitation is that non-zero G_{II} is obtained in spite

of the fact that the G_{II}/G_I ratio is almost zero. This might be attributed to the inherent limitations of the simple beam theory employed in the derivation of the proposed criterion.

Nevertheless, the proposed strain based criterion is very concise, simple and physically sound when designing bi-material bonded joints for mode I fracture testing. It is envisioned to be applicable for composite-composite, composite-metal and metal-metal bi-material joints.

7. Conclusions

A new design method to achieve mode I fracture is proposed and analysed for bonded DCB joints with two dissimilar adherends. It is identified that matching the longitudinal strain distributions of the two dissimilar adherends at the bondline eliminates mode II, and thus it provides pure mode I in the specimen.

The case study presented in this paper comprises two DCB configurations. In one of the configurations, the dissimilar adherends were designed to possess identical longitudinal strain distributions at the surfaces bonded with adhesive. The other configuration has two dissimilar adherends of the same flexural stiffness. VCCT technique is applied to model the fracture behaviour of the two DCB configurations, which is validated with experimental data. Both the experimental and modelling results show that approximately pure mode I is achieved by matching the longitudinal strain distributions. By contrast, the DCB configuration with matched flexural stiffness presents mode II fracture mode. The G_{II}/G_I ratio is reduced by a factor of 5 when using the proposed longitudinal strain based criterion in comparison with the flexural stiffness based criterion.

The DCB configuration with the identical flexural stiffness of two adherends provides false mode I fracture toughness values, as involved mode II fracture is overlooked in calculating the fracture toughness according to the ASTM D5528-13 standard. The mode I fracture toughness obtained can be therefore misleading. Matching the longitudinal strain distribution in the DCB specimen with dissimilar adherends is a general and more accurate approach to achieve pure mode I.

To minimize the mode II component in bonded bi-material joints where composite adherend is used, it is suggested to apply symmetric lay-up and minimize the difference in the flexural stiffnesses of two adherends.

Acknowledgement

This research was carried out under project number S32.6.14552a - Durabond in the framework of the Research Program of the Materials innovation institute (M2i) (www.m2i.nl) supported by the Dutch government.

References

[1] R. G. Boeman, D. Erdman, L. Klett, R. Lomax, A practical test method for mode I fracture toughness of adhesive joints with dissimilar substrates, in: SAMPE-ACCE-DOE Advanced Composites Conference, Detroit, USA, 1999, pp. 358–366.

[2] A. Vlot, J. W. Gunnink, Fibre metal laminates- an introduction, Kluwer Academic, Dordrecht, 2001.

[3] R. G. S. Barsoum, The best of both worlds : Hybrid ship hulls use composite & steel, The AMPTIAC Quarterly 7 (Number 3) (2003) 55–61.

[4] S. Teixeira de Freitas, J. Sinke, Failure analysis of adhesively-bonded skin-to-stiffener joints: Metalmetal vs. compositemetal, Engineering Failure Analysis 56 (2015) 2 – 13.

[5] S. Budhe, M. D. Banea, S. de Barros, L. F. M. da Silva, An updated review of adhesively bonded joints in composite materials, International Journal of Adhesion and Adhesives 72 (2017) 30–42.

[6] S. Teixeira de Freitas, M. Banea, S. Budhe, S. de Barros, Interface adhesion assessment of composite-to-metal bonded joints under salt spray conditions using peel tests, Composite Structures 164 (2017) 68 – 75.

[7] S. Teixeira de Freitas, J. Sinke, Adhesion properties of bonded composite-to-aluminium joints using peel tests, The Journal of Adhesion 90 (5-6) (2014) 511–525.

[8] S. Teixeira de Freitas, J. Sinke, Failure analysis of adhesively-bonded metal-skin-to-composite-stiffener: Effect of temperature and cyclic loading, Composite Structures 166 (2017) 27 – 37.

[9] C. D. Rans, R. C. Alderliesten, Damage tolerance philosophy for bonded aircraft structures, in: M. J. Bos (Ed.), Bridging the Gap between Theory and Operational Practice (ICAF2009), Springer Netherlands, Rotterdam, the Netherlands, 2009, pp. 73–90.

[10] ASTM D5528-13, Standard test method for Mode I interlaminar fracture toughness of unidirectional fiber-reinforced polymer matrix composites (2013).
[11] S. Azari, A. Ameli, M. Papini, J. K. Spelt, Analysis and design of adhesively bonded joints for fatigue and fracture loading: a fracture-mechanics approach, Journal of Adhesion Science and Technology 27 (15) (2013) 1681–1711.
[12] G. Ji, Z. Ouyang, G. Li, S. Ibekwe, S.-S. Pang, Effects of adhesive thickness on global and local Mode-I interfacial fracture of bonded joints, International Journal of Solids and Structures 47 (1819) (2010) 2445–2458.
[13] M. M. Shokrieh, M. Heidari-Rarani, M. R. Ayatollahi, Interlaminar fracture toughness of unidirectional dcb specimens: A novel theoretical approach, Polymer Testing 31 (1) (2012) 68–75.
[14] M. Cabello, A. Turon, J. Zurbitu, J. Renart, C. Sarrado, F. Martnez, Progressive failure analysis of dcb bonded joints using a new elastic foundation coupled with a cohesive damage model, European Journal of Mechanics - A/Solids 63 (2017) 22–35.
[15] M. S. Bin Mohamed Rehan, J. Rousseau, S. Fontaine, X. J. Gong, Experimental study of the influence of ply orientation on dcb mode-i delamination behavior by using multidirectional fully isotropic carbon/epoxy laminates, Composite Structures 161 (2017) 1–7.
[16] Z. Jiang, S. Wan, Z. Wu, Calculation of energy release rate for adhesive composite/metal joints under mode-i loading considering effect of the non-uniformity, Composites Part B: Engineering 95 (2016) 374–385.
[17] M. Khoshravan, F. Asgari Mehrabadi, Fracture analysis in adhesive composite material/aluminum joints under mode-i loading; experimental and numerical approaches, International Journal of Adhesion and Adhesives 39 (2012) 8–14.
[18] X. J. Gong, F. Hernandez, G. Verchery, Fracture toughness of adhesive bonded composite joints under mixed mode loading, in: 12th International Conference on Composites (ICCM12 Conference), Paris, France, 1999.
[19] Z. Ouyang, G. Ji, G. Li, On approximately realizing and characterizing pure mode-i interface fracture between bonded dissimilar materials, Journal of Applied Mechanics 78 (3) (2011) 031020–031020–11, 10.1115/1.4003366.
[20] G. Zambelis, T. D. S. Botelho, O. Klinkova, I. Tawfiq, C. Lanouette, Evaluation of the energy release rate in mode i of asymmetrical bonded composite/metal assembly, Engineering Fracture Mechanics 190 (2018) 175 – 185.
[21] J. G. Williams, On the calculation of energy release rates for cracked laminates, International Journal of Fracture 36 (2) (1988) 101–119.
[22] A. K. Kaw, Mechanics of composite materials, Taylor & Francis, Boca Raton, FL, USA, 2006.
[23] R. D. S. G. Campilho, A. M. G. Pinto, M. D. Banea, R. F. Silva, L. F. M. da Silva, Strength improvement of adhesively-bonded joints using a reverse-bent geometry, Journal of Adhesion Science and Technology 25 (2011) 2351–2368.
[24] G. Li, X. Wang, A. Li, W. Wang, L. Zheng, Fabrication and adhesive properties of thin organosilane films coated on low carbon steel substrates, Surface and Coatings Technology 201 (2007) 9571–9578.
[25] J. Pascoe, Delamination of bonded repairs-a damage tolerance approach, Master's thesis, Delft University of Technology, Delft, the Netherlands (2012).
[26] Z. Ye, P. V. Anastasios, K. Thomas, Mode i and ii fracture behavior of adhesively-bonded pultruded composite joints, Engineering Fracture Mechanics 77 (2010) 128–143.
[27] R. Krueger, Virtual crack closure technique: history, approach and applications, Applied mechanics reviews: American Society of Mechanical Engineers 57.
[28] S. Moslem, P. V. Anastasios, K. Thomas, Modelling effects of asymmetry and fiber bridging on mode i fracture behavior of bonded pultruded composite joints, Engineering Fracture Mechanics 99 (2013) 335–348.
[29] D. Zarouchas, R. Alderliesten, The effect of disbonds on stability aspects of adhesively bonded aluminum panels during compression loading, Thin-Walled Structures 96 (2015) 372 – 382. doi:https://doi.org/10.1016/j.tws.2015.07.027.
URL http://www.sciencedirect.com/science/article/pii/S0263823115300537
[30] E. S. Greenhalgh, Chapter 4 - delamination-dominated failures in polymer composites, in: Failure Analysis and Fractography of Polymer Composites, Woodhead Publishing, 2009, pp. 164–237.